Multi-Objective Optimization and Validation of a Diodic Profile

Avidh Bavkar[1], Peter Salek[2], Venkat Athmanathan[3], Guillermo Paniagua[4], Terrence Meyer[5]
Purdue University, West-Lafayette, Indiana, 47907, USA

James Braun[6]
North Carolina State University, Raleigh, North Carolina, 27695, USA

Hugh D. Perkins[7]
Nasa Glenn Research Center, Cleveland, OH 43315, USA

Chris Fugger[8]
Spectral Energies, Beavercreek, Ohio, 45430, USA

The present paper investigates the flow physics of Tesla valves and studies how various geometric parameters affect their performance. The performance of the valve is measured by its diodicity, evaluated by comparing pressure drops and discharge coefficients in the forward and reverse flow directions. First, only the flow return angle of a baseline geometry was varied to understand the impact of return angle on valve performance. These baseline geometries are first analyzed with CFD, and then fabricated and installed in a steady-state experimental test rig equipped with pressure transducers, to measure forward and reverse discharge coefficients. Seven additional geometries are also tested in cold flow to identify the impact of diode count, diode volume, and orifice size on valve performance. Next, a multi-objective optimizer is allowed to vary 12 geometric parameters to produce an optimum geometry.

I. Introduction

The diodic profile considered in this work is based on Nikola Tesla's Valvular Conduit, originally patented in 1920 [1]. This passive flow-control device uses a fixed internal geometry to promote low resistance to flow in one direction, but high resistance to flow in the opposite direction. The simplicity of this design has led it to be considered across many disciplines, including biomedical, agricultural, and aerospace. Previous optimizations of the Tesla valve can be found in literature: Bohm et al. generated elevated-diodicity valves at the microfluidic scale by performing a largely unconstrained topological multistage optimization [2]. At the macrofluidic scale, another topological optimization was performed in Gaymann et al. [3], including considerations for manufacturability of the geometry with additive techniques. Numerical analysis performed in Nobakht et al. show that the geometry of the junction between the reverse flow channel and the main flow channel is critical for valve performance [4]. Thompson et al. presents a numerical

---

[1] Undergraduate Student
[2] Research Assistant, AIAA Student Member
[3] Research Scientist, AIAA member
[4] Professor, AIAA Fellow
[5] Professor, AIAA Associate Fellow
[6] Assistant Professor, AIAA member
[7] Aerospace Research Engineer, Research and Engineering Directorate, AIAA Senior Member
[8] Research Engineer, AIAA senior member

technique to model flow inside a Tesla valve [5]. Gamboa et. al performed a 2-D optimization of a micro-scale diodic profile at low Reynolds numbers and identified the angle of injection of the secondary flow during reverse operation as a key parameter linked to valve performance [6]. This parameter was studied and investigated in our work as well. Nguyen et al. theorize that pulsatile flows have the potential to vastly improve valve performance in macrofluidic applications [7]. This feature is of particular interest in applications such as the one considered by Yang et. al, where Tesla-inspired valves were applied to inject a premixed kerosene-air mixture into a rotating detonation combustor [8] as well described by [9]. This study investigates the fluid dynamics of Tesla valves, utilizing a multi-objective optimization approach to enhance valve performance by modifying its geometry. Additionally, an experimental steady-state panel was built at Purdue University to calculate the diodicity of various injectors.

II. Performance Metrics

The discharge coefficient of a fluidic diode is a dimensionless parameter that quantifies the deviation of the actual mass flow rate from the theoretical mass flow rate through a straight tube under identical conditions. Mathematically, this coefficient is defined as the following ratio:

$$C_d = \frac{\dot{m}}{A\sqrt{2\rho\Delta P}}, \tag{1}$$

where $A, \dot{m}, \rho, \Delta P$, are the orifice area, actual mass flow rate, fluid density, and pressure drop respectively.

Hence, the discharge coefficient gives a way to measure the irreversible losses incurred as fluid transits through the diode. As the purpose of the fluidic diode is to minimize losses in the forward flow direction while enhancing losses in the reverse flow direction, the performance of a fluidic diode can be expressed in terms of the discharge coefficients computed in the forward and reverse flow directions, or alternatively by the pressure drop directly:

$$Di = \left(\frac{C_{d_{FWD}}}{C_{d_{REV}}}\right)^2 = \left(\frac{\Delta P_r}{\Delta P_f}\right)_{\dot{m}} \tag{2}$$

where $C_{d_{FWD}}$ and $C_{d_{REV}}$ are the forward and reverse discharge coefficients respectively [10].

III. Numerical Methodology

Through a multi-objective 2-D optimization approach, we aim to maximize the diodicity of the fluidic diode while simultaneously minimizing pressure loss in the forward flow direction. This optimization is controlled by the CADO multi-objective optimization tool [11]. The following procedure is conducted for each geometry:

A) Geometry is parametrically created from control variables in MATLAB®
B) 2D mesh generated with Numeca IGG™ and HEXpress™
C) Evaluation with Metacomp CFD++ [12]
D) Post processed in TecPlot®

In the following section, each of the above subroutines is further elaborated.

A. Parameterization of Diodic Profile

The following parameters of interest were identified for the parameterization and are sketched in Fig. 1:

- Inlet Width
- Outlet Width
- Center Width
- Length from inlet to center (L1)
- Length from center to outlet (L2)
- Angle of injection (θ)
- A series of control points generating recirculation lobe.

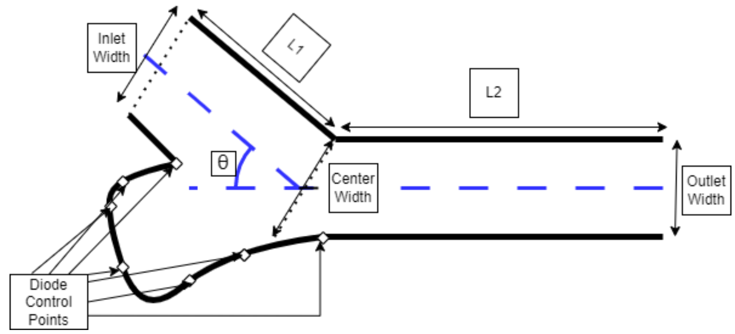

Fig. 1 Sketch of parameterization of diode.

The curve of the diode is defined by a modified Akima spline (MAKIMA interpolation in MATLAB®). The diodic valve is shown as parameterized in MATLAB® (Fig. 2). There is a parametric "centerbody" that can either be switched on or off. Two plenums are also included for the inlet and exhaust. A more constrained parameterization with the technique shown here is used for the main optimization (Fig. 13).

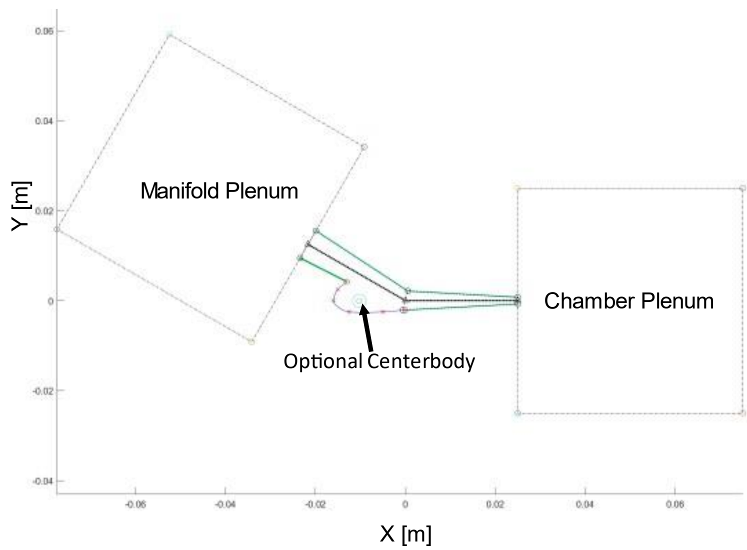

Fig. 2 Example geometry parameterized in MATLAB®

B. Meshing

The geometry is then exported from MATLAB® and meshed in Numeca HEXpress™, an unstructured mesher. A mesh inflation is applied along the viscous walls of the valve to capture the boundary layer, as can be seen in the close-up of Fig. 3. All meshing operations are scripted for automation, for use in the optimization step.

Additionally, a centerbody is added to divide the reverse flow. The centerbody can be enabled/disabled by the optimizer. A simple circular centerbody is shown in Fig. 3, but more complex center-bodies are used later on in the manuscript.

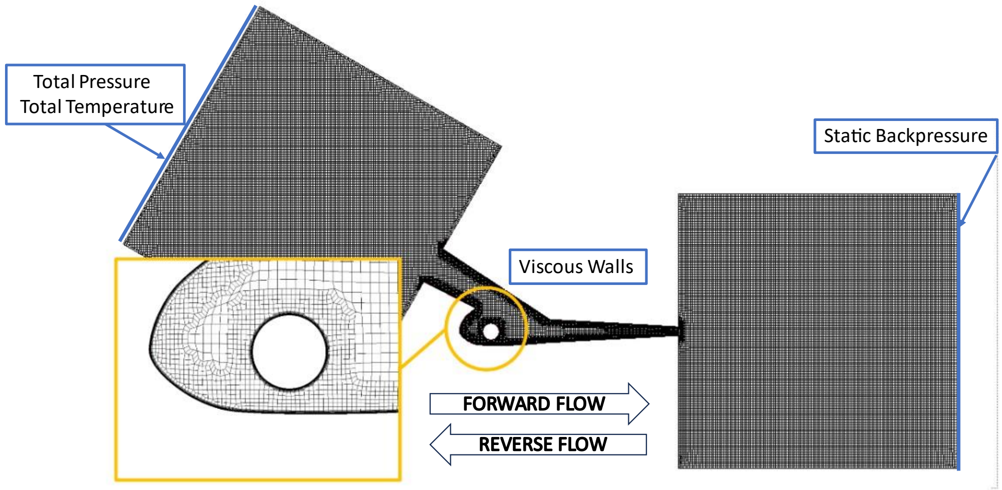

Fig. 3 Mesh with centerbody and CFD Boundary Conditions

C. 2-D CFD Evaluation and 1-D Validation

To evaluate the diodicity, two CFD runs are carried out for each geometry: one in the forward flow direction (left to right in Fig. 3) and one in the reverse flow direction (right to left in Fig. 3).

For the forward flow simulation, the boundary conditions are depicted in Fig. 3: A total pressure/temperature is imposed on the inlet, a simple back-pressure is imposed at the exit, and all other boundaries are treated as viscous adiabatic walls. For the reverse flow case, the total pressure/temperature and backpressure boundary conditions are simply swapped. The 2D Reynolds averaged Navier Stokes equations are solved, and for turbulence closure the k-omega-SST model is employed. Incompressible water is used as the fluid.

To ensure CFD produces appropriate results, a 1-D flow tool was created for both an incompressible liquid, assuming incompressible flow, and for a compressible gas, assuming isentropic flow. The different outputs that the tool outputs are shown in Fig. 4 for water and in Fig. 5 for air.

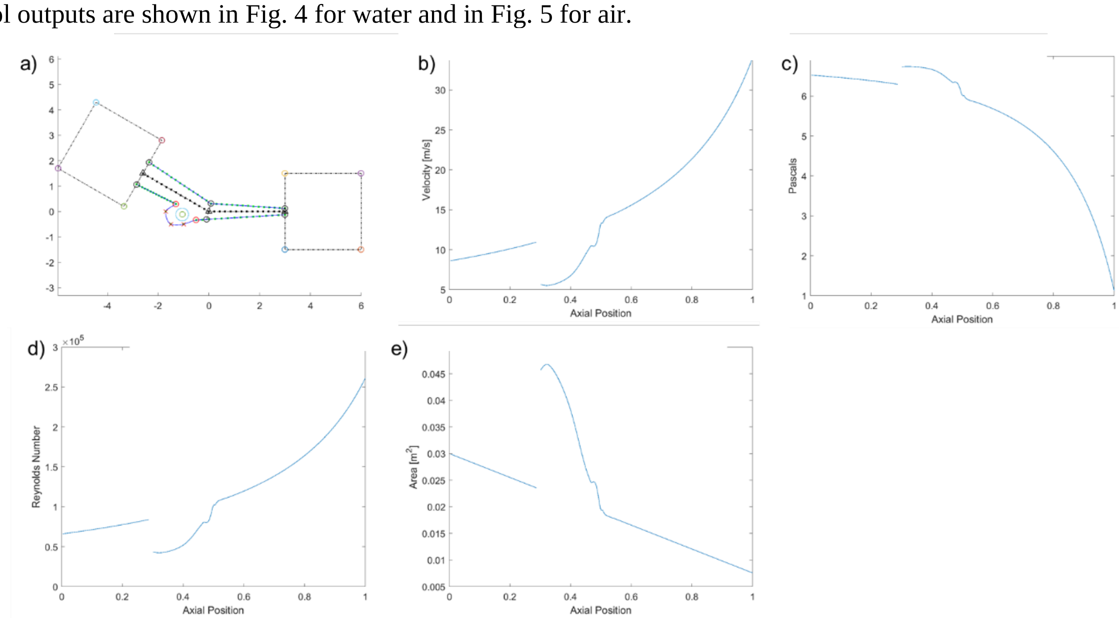

Fig. 4 Incompressible 1-D Tool. a) Geometry b) Velocity c) Pressure d) Reynolds Number e) Area

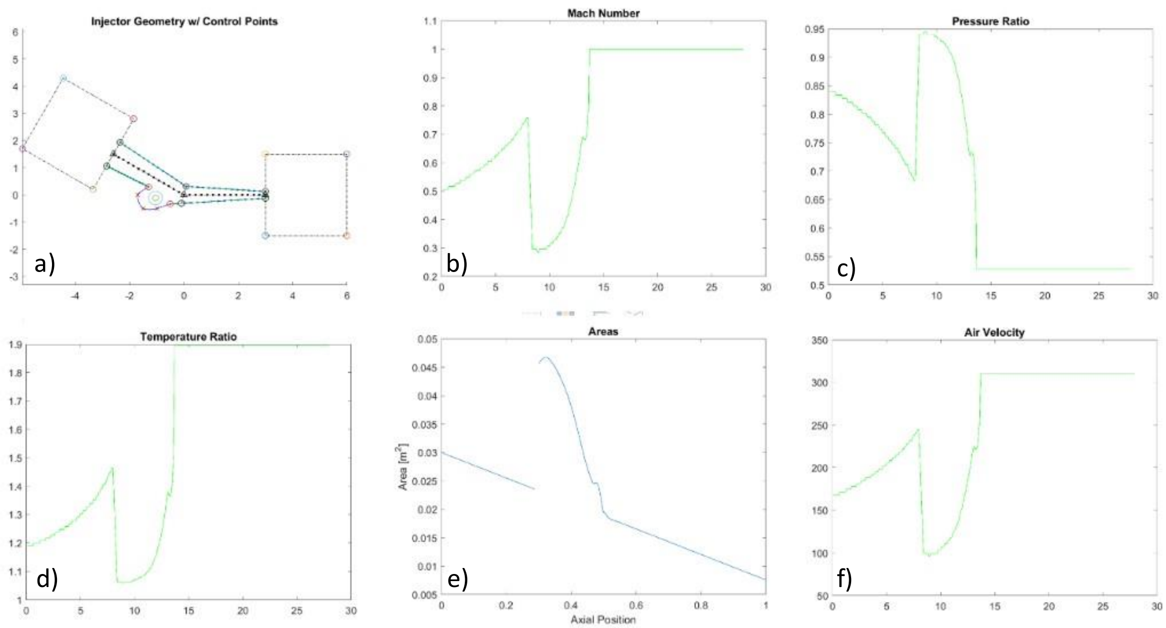

Fig. 5 Isentropic 1D Flow Tool a) Geometry b) Mach c) Pres. Ratio d) Temp. Ratio e) Area f) Velocity

D. Post Processing

A randomly selected, non-dimensional geometry was used as a CFD test case. An incompressible medium, water, was selected as the working fluid, with a manifold pressure of 3 bar and a chamber pressure of 1 bar for the forward flow case (Fig.6 a, b). In the reverse flow case, the boundary conditions for chamber and manifold were reversed, such that there was 3 bar in the chamber and 1 bar in the manifold. These cases are shown in Fig.6. For this particular geometry, the flow skips the lobe, resulting in a recirculation bubble (Fig.6 e).

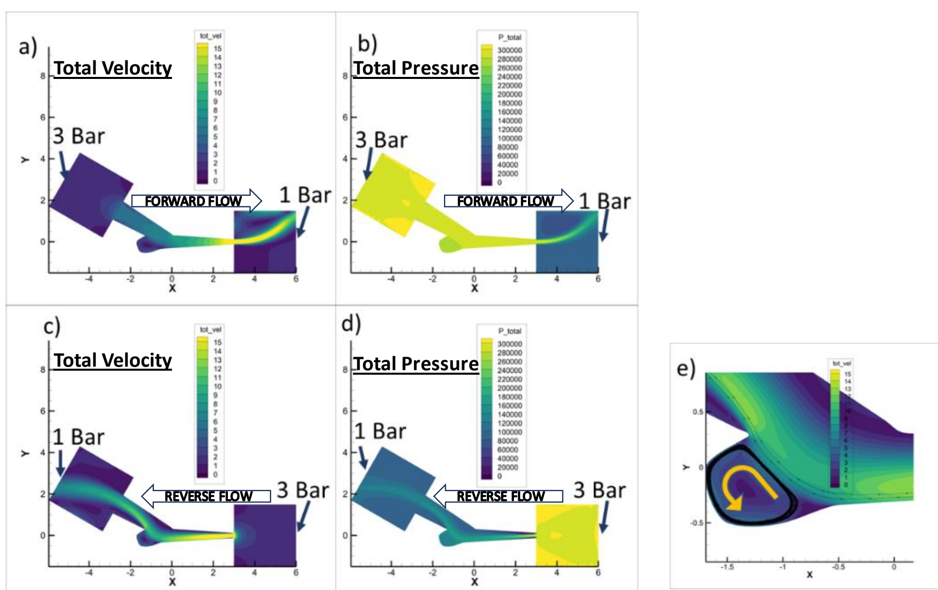

Fig. 6 Test Geometry CFD;
a) Velocity (Forward) b) Total Pressure (Forward)
c) Velocity (Reverse) d) Total Pressure (Reverse) e) Recirculation

IV. Experimental Methodology

A. Steady-State Test Rig

To experimentally evaluate fluidic diode performance, several 3-D printed plastic injectors are fabricated, each containing different diodic internal geometries. These injectors are evaluated at steady-flow conditions with the help of a steady-state test rig.

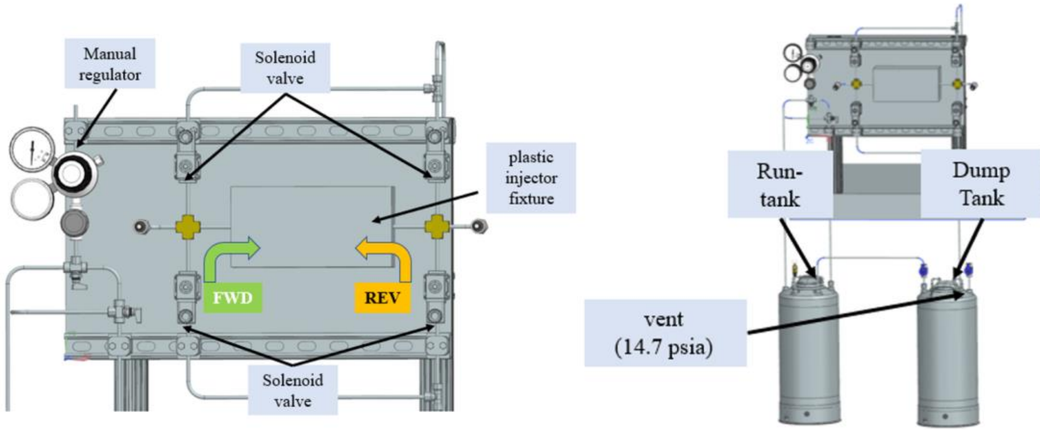

Fig. 7 CAD Model of steady-flow rig & water tanks

A schematic representation of the steady-state test rig along with the actual experimental setup is shown in Fig. 7. A manual regulator is used to set the ullage pressure of the run tank, which is filled with water. A set of four solenoid valves are used to control the flow direction through the injector which allow forward and reverse flow to be tested without having to remove the injector from the system. The dump tank collects water through the test to be pumped back into the run tank for subsequent tests.

The panel has a maximum nitrogen and water flow rate of 2265 SLPM and 9.1 SLPM respectively. The injectors can experience a max pressure ratio of 5.25 and can support a maximum orifice diameter of ~3 mm. The panel has a Coriolis flow meter for mass flow measurements, with a range up to 2 g/s precision and a precision <1%.

The entire testing and operation of the steady-flow rig is automated using a LabVIEW VI interface. The LabVIEW VI provides live estimates of the pressure drop, flow rate and the C_d for the injector. Based on the pressure drop set by the operator, the C_d value for the forward and reverse direction can be readily obtained through an automated test sequence. The valves are appropriately cycled to ensure a settling time and data acquisition time per experiment to obtain the steady flow discharge coefficient. This system is readily used for various pressure drops and flow rates of interest for the given injector. The uncertainty for the pressure transducers is +/- 1.0% and the Coriolis flow meter is +/- 0.1%. Using error propagation, the uncertainty for each of the calculated C_d values is +/- 0.71%.

V. Results

A. Experimental Evaluation

In parallel with the CFD optimization, the experimentally designed and fabricated set of injectors with diodic internal geometry. Diodic injectors were classified by three different parameters including number of diodes, volume of the diodes, and final orifice diameter. The baseline for this design of experiments consists of an injector with two diodes, medium volume, and a final orifice diameter, indicated as R_0". The parameters and reference numbers of all diode injectors can be seen in Table 1.

Table 1 Experimental Diode Injector Parameters

Injector #	Orifice Diameter(R_t)	Number of Diodes	Diode Size
2.1	R_0	2	Medium
2.2	$R_0/2$	2	Medium
2.3	$2R_0/390$	2	Medium

2.4	R_0	1	Medium
2.5	R_0	3	Medium
2.6	R_0	2	Small
2.7	R_0	2	Large

The diode is constructed by scaling a parametric axisymmetric spade design for the different diode sizes. The spade design is also scaled with respect to the radius of the orifice (Rt) as shown in Fig. 8. The volume of the diode is defined by the length of the diode (L), the radius of the diode (R), and the offset of the diode curve (S). Three diode volumes are initially selected, and the corresponding diode parameters are shown in Table 2**.**

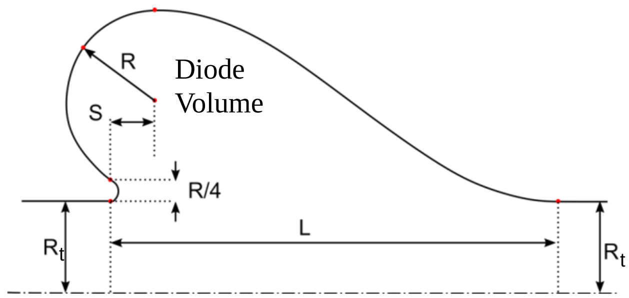

Fig. 8 Experimental Diode Parameterization

Table 2 Experimental Diode Volume Sizes

Diode Size (Volume)	L	R	S
Small	$3*R_t$	$0.75*R_t$	$R_t/2$
Medium	$4*R_t$	$1*R_t$	$R_t/2$
Large	$5*R_t$	$1.25*R_t$	$R_t/2$

Forward and reverse discharge coefficients are determined by several discrete pressure drops across the injector. Small variations in the achieved forward and reverse pressure drops may occur due to the difference in flow paths to the injector, which can lead to variations in flow associated total pressure loss. To account for this slight variation in the pressure drop within an individual test, data from the experiment is fitted with a polyfit curve, for the trends of forward and reverse C_d vs pressure drop.

This can be seen in Fig. 9a where the forward flow is represented by a positive pressure drop and the reverse is represented by a negative pressure drop. Each star represents a sample collected at that pressure drop, and the polyfit curve fitting procedure is applied separately to the forward and reverse C_d trends. This polyfit provides a continuous and smooth functional relationship between the discharge coefficient and the pressure drop across the injector. The diodicity vs pressure drop is calculated by using the ratio of the polyfit forward over reverse functions. The pressure dependent diodicity function is then plotted over the range over the experimental data, as seen in Fig. 9b.

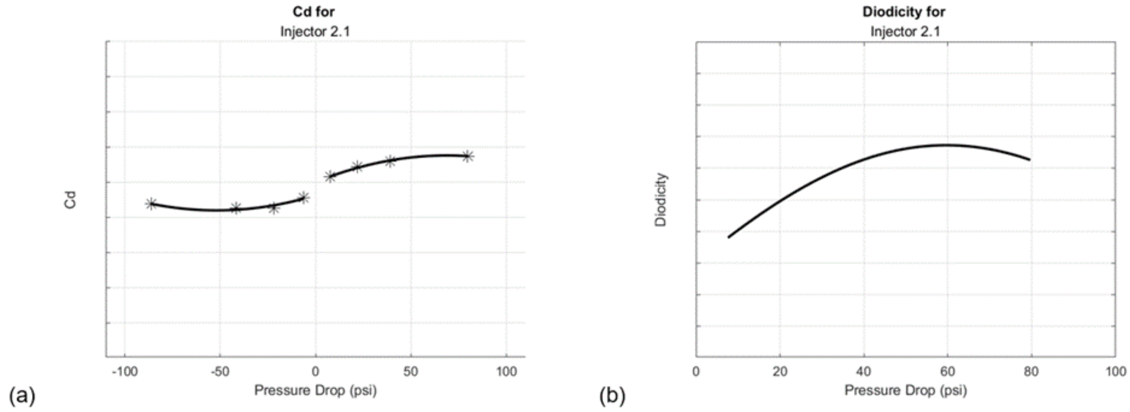

Fig. 9 a) C_d vs ΔP in forward and reverse direction b) Di vs ΔP for Injector 2.1

The functional dependence of number of diodes, volume of diodes, and orifice diameter on diodicity is explored in the steady state case. The impact of pressure drop on diodicity can be seen in Fig. 10a. Increasing the number of diodes provides a significant increase in the diodicity for a given pressure drop, however this change starts to plateau with increasing pressure drop across the injector.

With increasing diode volume, the diodicity starts to increase with increasing pressure drop. However, there appears to be a threshold volume for a given orifice size, beyond which the increase in diode volume seems to have negligible effect.

The orifice size appears to be impactful to injector behavior, but trends cannot be readily observed. This change can be attributed to the fact that in the current spade parameterization, various geometric parameters such as curvature and volume are affected by the orifice size.

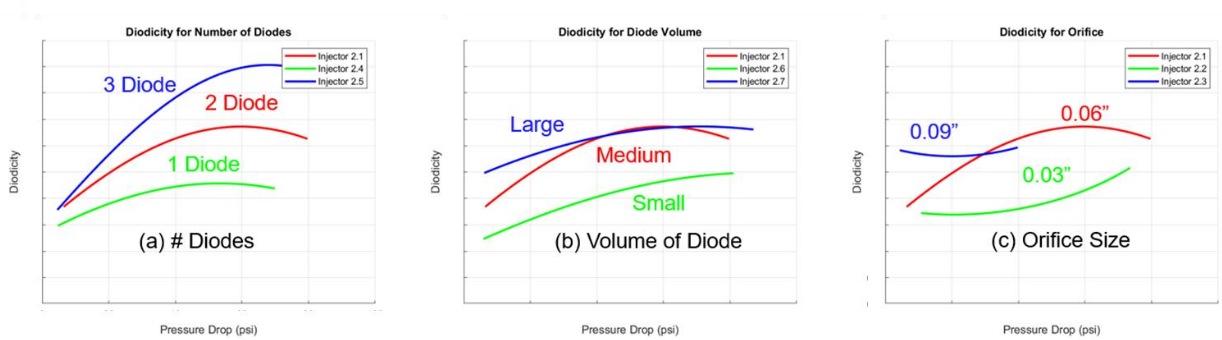

Fig. 10 Functional dependence on various parameters including:
(a) number of diodes, (b) volume of diodes, (c) orifice size (diodicity uncertainty +- 0.72%)

B. Numerical Baseline Geometry

To produce a baseline for further numerical optimization, the parameterization of Fig. 2 is adapted to generate geometries like those found in literature for Tesla valves. This adapted parameterization, shown in Fig. 13, constrains the diode wall into a semicircular shape and creates a concentric centerbody, which together make a return channel for the reverse flow to travel through. The geometry of the diode and centerbody is controlled by the channel width, expressed as a percentage of the center diameter, as well as the return angle, which describes the angle that the reverse flow moving through the return channel is injected into the main flow.

In the experiments performed by Gamboa et. al., there is a high correlation between the flow return angle and the diodicity. To explore this, two geometries were assessed, one with a high flow return angle and one with a low flow return angle. This baseline geometry is an attempt to scale the geometry presented in Gamboa et. al. to match the inlet and outlet diameters that match those tested by the experimental team in cold-flow testing. The boundary conditions for this run as well as all subsequent optimization steps remain unchanged: Water is used as the fluid with a 3 Bar total pressure upstream and 1 bar back pressure downstream.

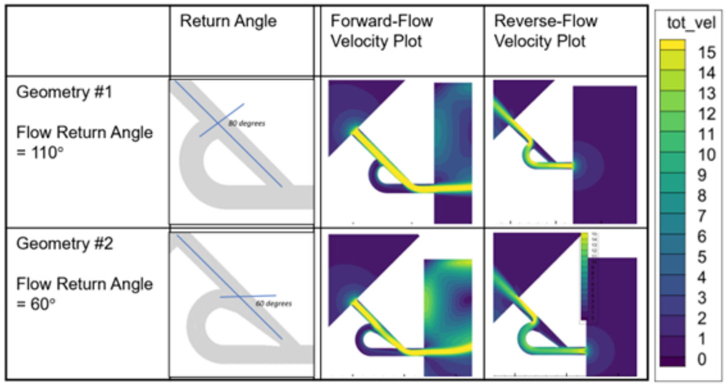

Fig. 11 Comparison of baseline geometries at different flow return angles.

In line with the results from Gamboa et. al, the low flow return angle case (Geometry #2) featured enhanced performance, showing a 17% improvement in diodicity over Geometry #1.

C. Experimental Validation of the Numerical Baseline

The baseline geometries described above in Fig. 11 were manufactured and tested in accordance with the steady state testing outline described above. The diodicity vs pressure drop curve for these injectors can be seen in Fig. 12. As calculated by the RANS CFD models, geometry #2 outperforms geometry #1.

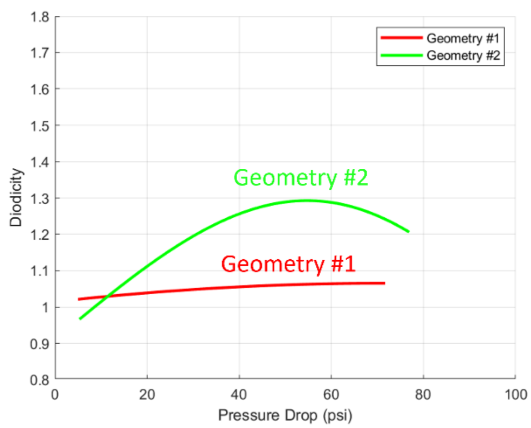

Fig. 12 Experimental *Di* vs Δ*P* for baseline geometries #1 & #2 (diodicity uncertainty +- 0.72%)

D. CFD Optimized Geometry

In pursuit of additional improvements to the valve geometry, a multi-objective optimization routine was implemented. To allow more freedom in the geometries considered, the parameterization was modified based on the baseline results. For the optimization, the inlet, outlet, and center widths are all held constant, while the inclination angle and the flow return angle are allowed to vary. Furthermore, 5 control points are placed on both the diode and the center body, allowing the geometry of the return passage to vary. These parameters and an example geometry are shown in Fig. 13 and Table 3.

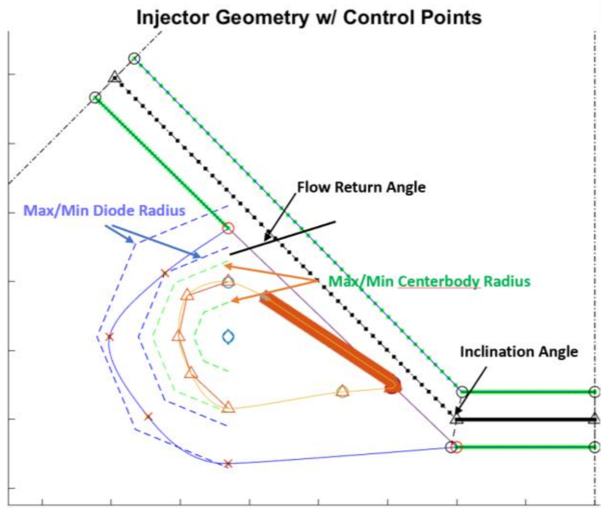

Fig. 13 Diode Parameterization for Numerical Optimization

Table 3 Parameterization Variables for Optimization

Variable(s)	Variable Number	Minimum	Maximum
Flow Return Angle	1	0°	60°
Diode Radial Perturbation Control Points 1-5	2, 3, 4, 5, 6	-75% of channel	+75% of channel
Centerbody Radial Perturbation Control Points 1-5	7, 8, 9, 10, 11	-75% of channel	+75% of channel
Inclination Angle	12	0°	60°

For the initial design of experiments, the inclination angle was fixed at 45 degrees, and 64 individuals were generated through a fractional factorial approach. Fig. 14a shows the discharge coefficient of these individuals. Fig. 14b shows the results full optimization, showing all 393 individuals that were run. The optimization objectives were set to maximize the forward C_d and elevate the diodicity. A pareto front is found where individuals have both elevated forward and reverse C_d , however individuals with elevated forward C_d and low reverse C_d are also found, those featuring elevated diodicity.

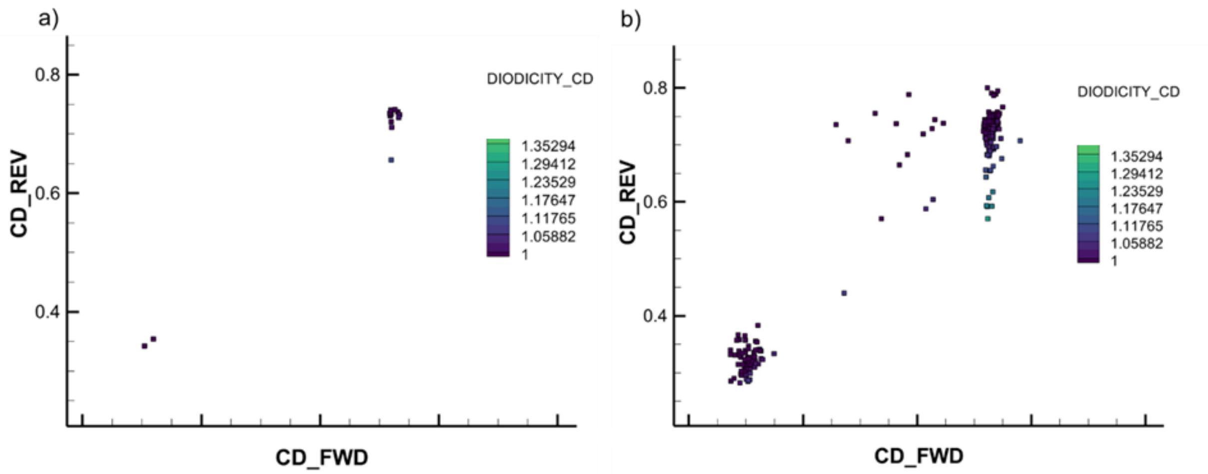

Fig. 14 a) Discharge coefficient initial run (n=64) b) Discharge coefficients full optimization (n=393)

Fig. 15 depicts a poor performing individual from the optimization with low diodicity and an elevated forward Cd of 0.75. It can be seen in this geometry that the flow travelling in the reverse direction flows via the main path rather than the diodic lobe, resulting in poor reverse-flow resistance and low diodicity. The mass flow convergence of these CFD runs is given in Fig. 16.

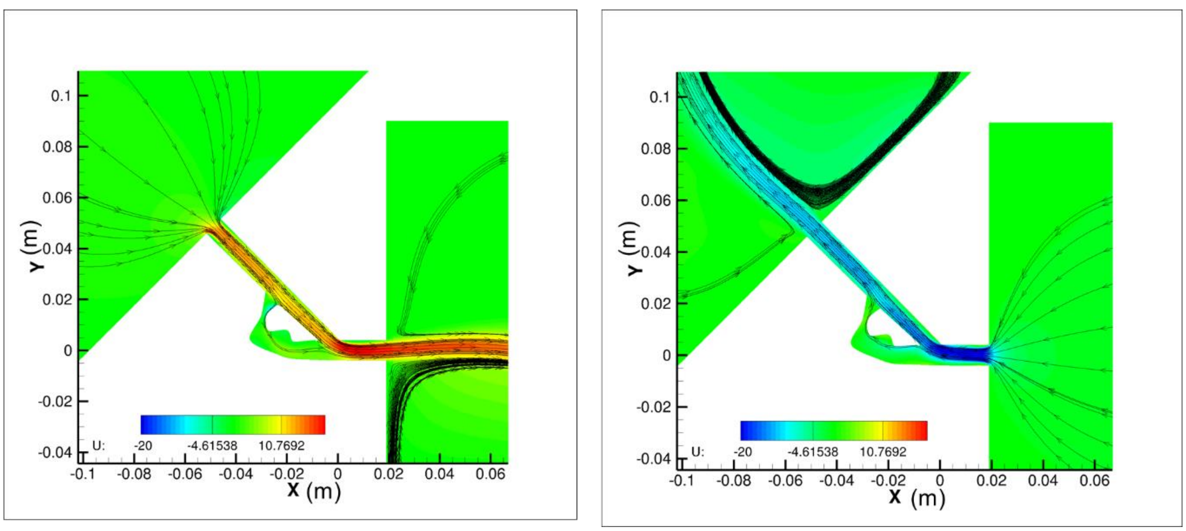

Fig. 15 Low diodicity individual. Forward Flow (Left) & Reverse Flow (Right)

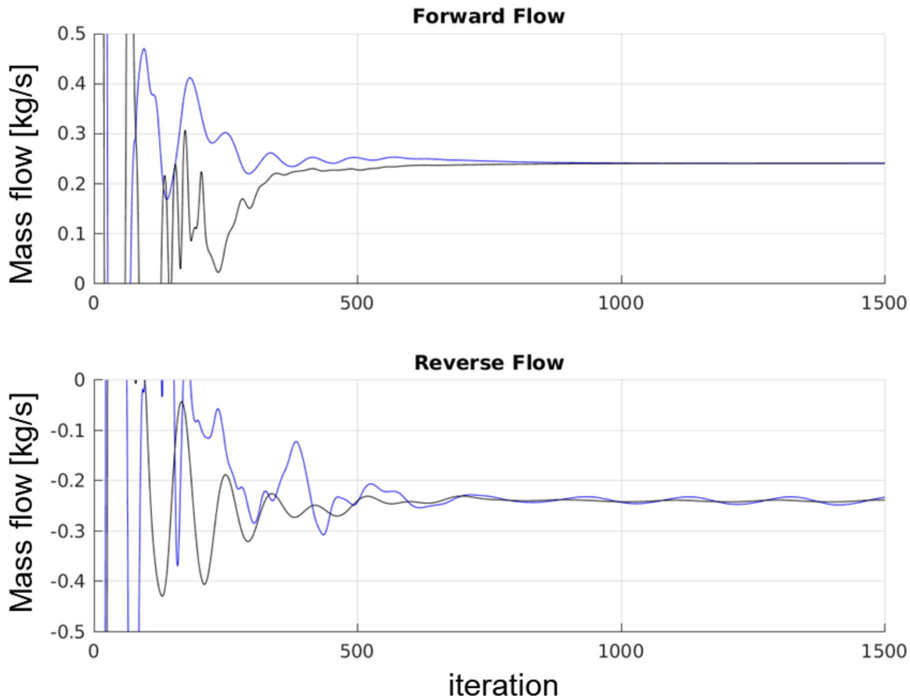

Fig. 16 Mass flow convergence for low diodicity individual

However, it was observed that the CFD simulations of certain individuals had difficulty with convergence due to extreme geometry features like sharp corners that induced separation within the diode. To remedy this, the interpolation of the centerbody was changed from an Akima-spline to a Bezier based interpolation, resulting in the smoother centerbody shown in Fig. 17.

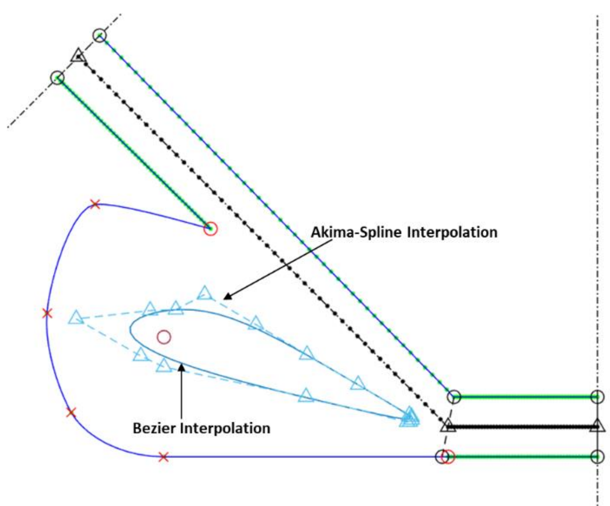

Fig. 17 Comparison of Bezier vs Akima-Spline Interpolation on randomly selected individual to improve CFD convergence.

Alternately, Fig.. 18 depicts an elevated performing individual. In contrast to the previous individual, most of the reverse flow is directed through the diodic lobe rather than the main path. Additionally, it was observed that all geometries with elevated diodicity featured a high return angle.

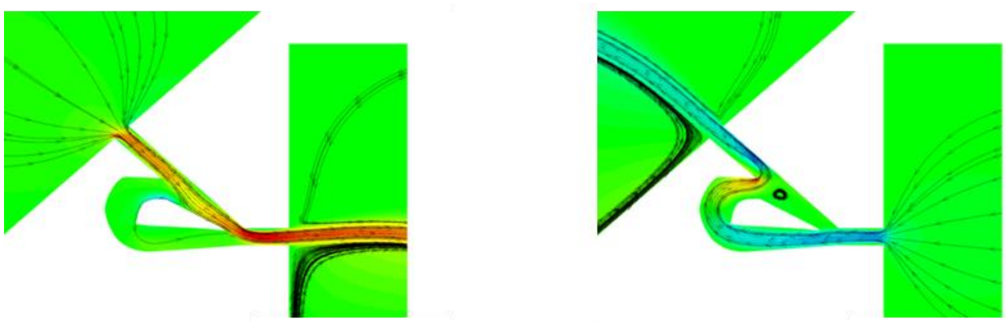

Fig.. 18: Elevated Diodicity Individual: forward case (left) and reverse case (right)

This trait is exemplified in Figure 19, where all 393 individuals are color-marked according to their return angle. Elevated-diodicity individuals, with a low reverse Cd and elevated forward Cd, often feature a high return angle.

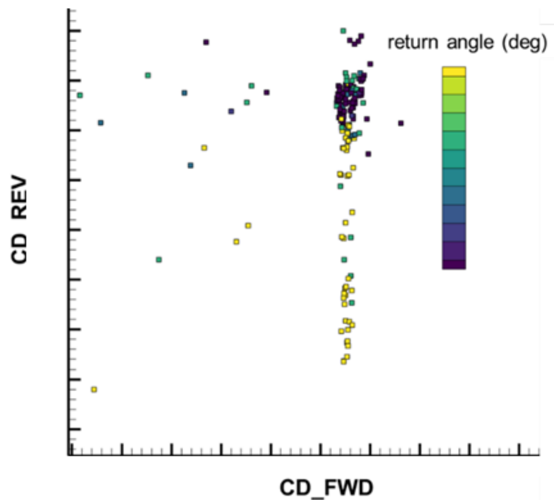

Figure 19: Influence of the Return Angle

Finally, the inclination angle of the valve was allowed to vary between 0 and 60 degrees. As the inclination is lowered, higher discharge coefficients in both directions are observed. One such individual is shown in Figure 20(right). However, at lower inclinations, large oscillations in mass-flow are detected (Figure 21).

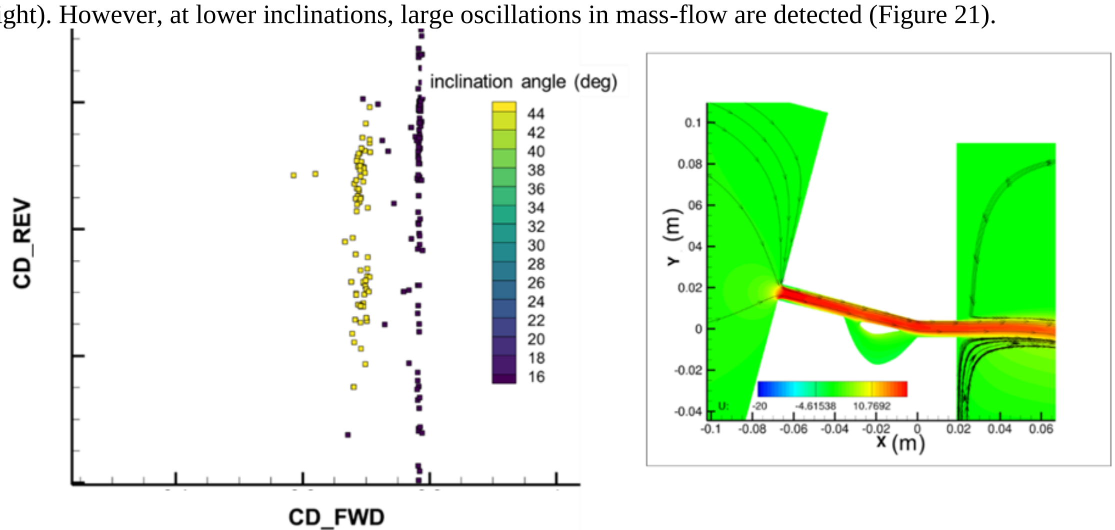

Figure 20 optimization with varying inclination angle: plot of forward Cd vs reverse Cd (left), and a geometry with low inclination angle with forward flow (right)

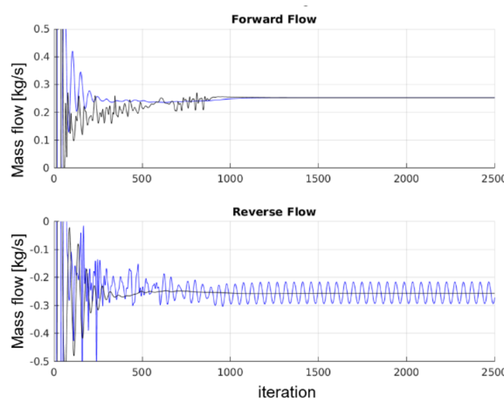

Figure 21: Mass Flow as function of the iteration step for the forward (top) and reverse flow (bottom)

VI. Conclusions

In this work, we have devised an approach and developed the tools to improve the geometry of a diodic profile for steady incompressible fluids, inspired by the geometry of a Tesla valve. Several parameterization strategies have been described to provide flexibility in profile geometry with a minimum number of parameters, and an optimization was carried out numerically to understand the parameters that promote elevated-diodicity designs. We have found that the angle at which the reverse flow in the diodic passage impinges upon the main flow path (flow-return angle in our discussion above) should be maximized, and the geometry should be shaped to allow most of the reverse flow to transit through the diodic passage. The numerical tools were validated and additional parameters such as diode count were investigated by experimental testing of 3-D printed diodic profiles in a steady-state cold-flow test-rig. Specifically, two geometries from the computational analysis were manufactured and tested, and the observed improvements from the CFD were confirmed by the experiments.

Acknowledgements

We would also like to thank Krishna Nagarajan for supporting the experimental efforts. This work was funded by NASA SBIR contracts 80NSSC22PB194 and 80NSSC23CA152

References

[1] Tesla, N. (1920). *Valvular conduit* [Review of *Valvular conduit*]. https://patents.google.com/patent/US1329559A/en
[2] Bohm, S., Phi, H. B., Moriyama, A., Runge, E., Strehle, S., König, J., Cierpka, C., and Dittrich, L., "Highly Efficient Passive Tesla Valves for Microfluidic Applications," Microsystems & Nanoengineering, Vol. 8, No. 1, 2022, pp. 1–12. https://doi.org/10.1038/s41378-022-00437-4
[3] Gaymann, A., Montomoli, F., and Pietropaoli, M., "Design for Additive Manufacturing: Valves Without Moving Parts," presented at the ASME Turbo Expo 2017: Turbomachinery Technical Conference and Exposition, Charlotte, North Carolina, USA, 2017. https://doi.org/10.1115/GT2017-64872
[4] Nobakht, A. Y., Shahsavan, M., and Paykani, A., "Numerical Study of Diodicity Mechanism in Different Tesla-Type Microvalves," Journal of Applied Research and Technology, Vol. 11, No. 6, 2013, pp. 876–885. https://doi.org/10.1016/S1665-6423(13)71594-3
[5] Thompson, S. M., Jamal, T., Paudel, B. J., & Walters, D. K. (2013). Transitional and Turbulent Flow Modeling in a Tesla Valve. *Volume 7B: Fluids Engineering Systems and Technologies*. https://doi.org/10.1115/imece2013-65526
[6] Gamboa, A. R., Morris, C. J., & Forster, F. K. (2004). Improvements in fixed-valve micropump performance through shape optimization of valves. *Journal of Fluids Engineering*, *127*(2), 339–346. https://doi.org/10.1115/1.1891151
[7] Nguyen, Q. M., Abouezzi, J., & Ristroph, L. (2021). Early turbulence and pulsatile flows enhance diodicity of Tesla's macrofluidic valve. *Nature Communications*, *12*(1). https://doi.org/10.1038/s41467-021-23009-y

[8] Yang, X., Wu, Y., Song, F., Zhou, J., Liu, H., Xu, S., & Chen, X. (2023). Experimental study on a premixed rotating detonation combustor using Tesla inlet configuration fueled by kerosene. *Experimental Thermal and Fluid Science*, *146*, 110928. https://doi.org/10.1016/j.expthermflusci.2023.110928
[9] Teasley, T.W., Protz, C.S., Larkey, A.P., Williams, B.B. and Gradl, P.R., 2021. A Review Towards the Design Optimization of High Performance Additively Manufacthttps://doi.org/10.2514/6.2021-3655ured Rotating Detonation Rocket Engine Injectors. In AIAA Propulsion and Energy 2021 Forum (p. 3655).
[10] Keller, A. R., Otomize, J., Nair, A. P., Minesi, N. Q., and Spearrin, R. M., "High-Diodicity Impinging Injector Design for Rocket Propulsion Enabled by Additive Manufacturing," 2022. https://doi.org/10.2514/6.2022-1265
[11] Verstraete T, Alsalihi Z, Van den Braembussche R. Multidisciplinary optimization of a radial compressor for microgas turbine applications. J Turbomach 2010;132(3):031004. doi: 10.1115/1.3144162
[12] Chakravarthy S, Peroomian O, Goldberg U, Palaniswamy S. The CFD ++ computational fluid dynamics software suite. AIAA and SAE. World Aviation Conference Anaheim, CA; 1998. doi: 10.2514/6.1998-5564